RSC Advances

PAPER

View Article Online
View Journal | View Issue

Cite this: *RSC Adv.*, 2026, **16**, 15490

Ni–Fe bimetallic carbon nanotube catalysts derived from a two-dimensional metalloporphyrin Fe-MOF precursor for oxygen reduction and oxygen evolution reactions

Yunyang Wu *

Oxygen reduction reaction (ORR) and oxygen evolution reaction (OER) are critical half-reactions in energy conversion devices such as metal–air batteries and reversible fuel cells, and their sluggish kinetics severely limit the overall device performance. Therefore, the development of efficient, stable, and low-cost non-precious metal bifunctional electrocatalysts is of great significance. In this study, a MOF-derived bifunctional electrocatalytic material (NiFe@CNT), featuring NiFe bimetallic alloys uniformly anchored within a carbon nanotube network, was successfully fabricated using a two-dimensional metalloporphyrin-based Fe-MOF precursor *via* metal site modulation by introducing Ni, combined with a high-temperature pyrolysis strategy. Structural characterization results indicate that NiFe@CNT possesses an intact three-dimensional CNT conductive network, a high degree of graphitization (I_D/I_G = 0.39), and uniformly dispersed NiFe alloy active phases. Electrochemical evaluations reveal that NiFe@CNT functions as a highly active bifunctional catalyst for both ORR and OER in alkaline environments. Regarding its ORR activity, the material exhibits a half-wave potential comparable to that of benchmark Pt/C, with reaction kinetics proceeding through an approximately four-electron transfer mechanism. In terms of OER performance, a current density of 10 mA cm^{-2} is attained at a modest overpotential of merely 1.514 V. In alkaline electrolyte, the ORR proceeds predominantly through a four-electron pathway converting O_2 to H_2O ($O_2 + 4H^+ + 4e^- \rightarrow 2H_2O$), while the OER involves the reverse four-electron oxidation of hydroxide to produce molecular oxygen ($2H_2O \rightarrow O_2 + 4H^+ + 4e^-$). Furthermore, durability assessments confirm that NiFe@CNT surpasses commercial noble metal benchmarks in long-term operational stability. This work presents a viable approach for fabricating advanced noble-metal-free oxygen electrocatalysts through two-dimensional MOF-derived engineering.

Received 24th February 2026
Accepted 14th March 2026

DOI: 10.1039/d6ra01624c

rsc.li/rsc-advances

1 Introduction

The oxygen reduction reaction (ORR) and oxygen evolution reaction (OER) have been extensively investigated because of their central roles in renewable energy conversion technologies such as reversible fuel cells and metal–air batteries, particularly zinc–air batteries, which have attracted significant attention due to their high theoretical energy density and environmental compatibility.[1–4] However, the intrinsically sluggish kinetics of both reactions severely limit overall energy conversion efficiency.[5–7] At present, high-performance ORR and OER catalysts still rely predominantly on noble-metal-based materials, including Pt and Ir/Ru oxides. Although these catalysts exhibit excellent catalytic activity, their high cost, limited availability, and insufficient long-term stability significantly hinder large-scale industrial implementation.[8,9] Consequently, the development of efficient, durable, and low-cost bifunctional catalysts based on non-noble metals has emerged as a major research focus in this field.[10]

In recent years, catalysts derived from metal–organic frameworks (MOFs) have attracted considerable attention in ORR/OER electrocatalysis owing to their tunable structures, large specific surface areas, and unique capability to construct high-density, atomically dispersed metal active sites.[11–13] For instance, Li *et al.* reported a Fe–N–C/rGO catalyst containing FeN_5 atomic sites, synthesized *via* the pyrolysis of graphene oxide and ZIF-8. The asymmetric electron-deficient region located above the metal center of the FeN_5 site was shown to effectively modulate the adsorption energies of reaction intermediates, thereby markedly lowering the reaction energy barriers for both ORR and OER and enhancing the overall catalytic activity. This work convincingly demonstrated the substantial potential of MOF-derived materials for the rational design of high-performance bifunctional catalysts.[14,15] Among various metal-based MOFs, iron-based metal–organic

College of Polymer Science and Engineering, Sichuan University, Chengdu 610040, China. E-mail: wuyunyang@stu.scu.edu.cn

frameworks (Fe-MOFs) have received particular attention due to their favorable physicochemical properties and the natural abundance of iron resources.[16–19] Chang *et al.* developed a Fe_3C/Fe–N–C catalyst *via* a Fe single-atom seed-mediated strategy, which exhibited outstanding bifunctional ORR/OER activity. Notably, this catalyst delivered a lower ΔE value during ORR/OER operation than Pt/C + RuO_2 and other reference catalysts, further confirming the remarkable promise of Fe-based MOFs in bifunctional electrocatalysis.[20]

Although single-atom catalysts have demonstrated outstanding activity toward either ORR or OER, their bifunctional catalytic performance is often intrinsically constrained due to the limited ability of isolated active sites to simultaneously optimize the adsorption energies of different reaction intermediates.[21] In particular, isolated active sites are often unable to cooperatively promote ORR and OER simultaneously, and the adsorption strengths of key intermediates such as OOH* and OH* cannot be optimized in a balanced manner on a single site. These limitations collectively restrict the overall bifunctional catalytic efficiency of single-atom systems.[22–24] The limited bifunctional activity of single-atom catalysts mainly arises from the intrinsic difficulty of simultaneously optimizing the adsorption energies of key reaction intermediates involved in ORR and OER. During ORR, efficient catalysis requires moderate adsorption of oxygenated intermediates such as OOH* to facilitate electron transfer and O–O bond cleavage. In contrast, OER involves the sequential oxidation of hydroxyl intermediates such as OH*, O*, and OOH*. The optimal binding energies of these intermediates often differ significantly. As a result, a single isolated metal site typically cannot provide an ideal adsorption environment for all intermediates involved in both reactions. This limitation restricts the bifunctional catalytic efficiency of single-atom systems and motivates the development of multi-metal or cooperative catalytic sites. Compared with monometallic MOFs, bimetallic MOFs generally exhibit larger specific surface areas (typically 20–50% higher than their monometallic counterparts),[25,26] a greater density of tunable active sites, and significantly improved electrical conductivity due to the synergistic electronic interactions between the two metal centers. More importantly, the synergistic interactions between two different metal species endow bimetallic MOFs with superior catalytic activity.[27–30] Among various transition metals, nickel is abundant in nature and possesses excellent corrosion resistance, high ductility, and favorable electrochemical properties, which have enabled its widespread application in batteries, water splitting, and other redox-related fields.[31–33] In addition, a growing body of evidence suggests that the coexistence of Fe and Ni leads to strong electronic and structural interactions, thereby imparting the system with enhanced ORR/OER performance.[34–38] Cheng *et al.* successfully fabricated a highly active and durable bimetallic NiFe-MOF bifunctional oxygen electrocatalyst using a photo-induced lattice strain strategy. The resulting catalyst exhibited ORR/OER activities far exceeding those of conventional MOFs and even commercial noble-metal catalysts. *In situ* characterization further revealed that the Fe/Ni dual-metal sites jointly drive an efficient four-electron reaction pathway, highlighting the significant application potential of Fe/Ni bimetallic MOFs.[39] In alkaline media, the ORR can proceed through two principal pathways: a two-electron pathway producing hydrogen peroxide ($O_2 + 2H^+ + 2e^- \rightarrow H_2O_2$), and a more desirable four-electron pathway in which oxygen is directly reduced to water ($O_2 + 4H^+ + 4e^- \rightarrow 2H_2O$).[40,41] The four-electron pathway is generally preferred because it provides higher energy efficiency and suppresses peroxide formation.[42] The OER corresponds to the reverse process, involving a four-electron oxidation of hydroxide ions to produce molecular oxygen ($2H_2O \rightarrow O_2 + 4H^+ + 4e^-$).[43] The catalytic pathway and kinetics of these reactions are strongly influenced by the electronic structure and coordination environment of active sites in MOF-derived catalysts. In particular, Fe–N coordination sites can effectively activate molecular oxygen, while the introduction of Ni species can regulate the electronic structure of Fe centers and optimize the adsorption energies of reaction intermediates such as OOH* and OH*, thereby promoting the four-electron ORR pathway.

Conventional MOF materials are predominantly three-dimensional, and their practical applications are often hampered by poor electrical conductivity and incomplete exposure of active sites.[44–47] In contrast, two-dimensional MOFs not only retain the high porosity and structural tunability of their three-dimensional counterparts, but also benefit from extended conjugated frameworks that facilitate electron transport, thereby exhibiting considerable promise in ORR/OER electrocatalysis.[48] Nevertheless, the application of 2D MOFs in this field remains challenging. On the one hand, bimetallic MOFs often suffer from limited structural stability.[49,50] On the other hand, their synthesis is inherently demanding, as nonuniform metal distribution can induce phase separation or crystallographic defects.[49] Moreover, the randomness and poor predictability associated with constructing dual-metal sites in 2D MOFs make precise regulation of active sites particularly difficult.[48]

In this work, a Ni-modified two-dimensional metal-porphyrin-based Fe-MOF precursor was rationally designed and synthesized, followed by the preparation of a series of bimetallic catalysts through optimization of the pyrolysis process. The morphology, crystalline structure, pore characteristics, and elemental valence states of the resulting materials were systematically characterized using SEM, TEM, XRD, BET, and XPS. Their ORR and OER electrochemical performances were then evaluated in a three-electrode configuration and benchmarked against a commercial Pt/C catalyst to assess bifunctional activity. By establishing an integrated research framework spanning molecular design, material fabrication, and performance validation, this study is expected to advance the application of MOF-derived materials in energy conversion and to contribute to the development of efficient and stable electrochemical devices. Therefore, the aim of this study is to develop an efficient bifunctional electrocatalyst derived from a two-dimensional metalloporphyrin Fe-MOF precursor through bimetallic modulation with Ni. The specific tasks include: (i) synthesizing NiFe-MOF and ZnFe-MOF precursors; (ii) constructing MOF-derived carbon nanotube composite catalysts *via* controlled pyrolysis; (iii) systematically

characterizing their structural and electronic properties; and (iv) evaluating their bifunctional catalytic performance for ORR and OER in alkaline media.

2 Materials and methods

2.1 Chemicals

All chemicals were of analytical grade and used without further purification. 4,4′-Bipyridine (99%), nickel nitrate hexahydrate ($Ni(NO_3)_2 \cdot 6H_2O$, ≥98%), zinc nitrate hexahydrate ($Zn(NO_3)_2 \cdot 6H_2O$, ≥98%), and polyvinylpyrrolidone (PVP, $M_w \approx 40\,000$) were purchased from Aladdin Reagent Co., Ltd (Shanghai, China). 5,10,15,20-Tetrakis(4-carboxyphenyl)porphyrin iron(III) (FeTCPP, ≥97%) and H_2TCPP were obtained from Sigma-Aldrich. Carbon nanotubes (CNTs, purity > 95%) were supplied by Timesnano Co., Ltd (Chengdu, China). Nafion solution (5 wt%) and commercial Pt/C catalyst (20 wt%) were purchased from Alfa Aesar. Ethanol and *N*,*N*-dimethylformamide (DMF) were analytical grade reagents obtained from Sinopharm Chemical Reagent Co., Ltd.

2.2 Preparation of NiFeMOF, ZnFeMOF, and NiMOF

4,4′-Bipyridine (2.34 mg, 0.015 mmol), $Ni(NO_3)_2 \cdot 6H_2O$ (2.91 mg, 0.01 mmol), and polyvinylpyrrolidone (10 mg) were dissolved in a DMF/ethanol solution (v/v = 3 : 1, 6 mL). Meanwhile, 5,10,15,20-tetrakis(4-carboxyphenyl)porphyrin iron(III) (FeTCPP) (4.2 mg, 0.005 mmol) was dissolved in a DMF/ethanol solution (v/v = 3 : 1, 2 mL) to obtain a FeTCPP solution. The FeTCPP solution was added dropwise into a 10 mL glass vial containing the initial mixture, followed by sonication for 15 min. The mixture was then heated to 80 °C and allowed to react for 20 h, yielding a brown precipitate. The precipitate was collected by centrifugation, washed sequentially with ethanol and dichloromethane, and then dried overnight in a vacuum oven at 60 °C to obtain the target product, denoted as NiFeMOF.

To investigate the respective roles of Ni^{2+} and the $Fe–N_4$ centers in the resulting NiFeMOF, control samples were prepared using identical procedures. Specifically, ZnFeMOF was synthesized by replacing $Ni(NO_3)_2$ in the above solution with $Zn(NO_3)_2$, and NiMOF was prepared by substituting FeTCPP with H_2TCPP (metal-free 5,10,15,20-tetrakis(4-carboxyphenyl) porphyrin).

2.3 Preparation of NiFe@CNT, ZnFe@CNT, and Ni@CNT

NiFeMOF (100 mg) and carbon nanotubes (CNT; 100 mg) were placed separately at the bottom of a porcelain boat and gradually heated from 25 °C to 300 °C at a rate of 5 °C min^{-1} under a nitrogen atmosphere. The temperature was maintained at 300 °C for 2 h, and then further increased at the same heating rate from 300 °C to the optimal 700 °C and held for 4 h to complete the pyrolysis process. After pyrolysis, the product was cooled to 25 °C, yielding a black powder of NiFe@CNT (approximately 50 mg). The same procedure was applied to pyrolyze ZnFeMOF and NiMOF to obtain ZnFe@CNT and Ni@CNT, respectively.

2.4 Characterization

The morphological features of the as-prepared samples were examined using field-emission scanning electron microscopy (FE-SEM, Sigma 360, ZEISS, Germany). To gain deeper insight into the internal microstructure, transmission electron microscopy (TEM, JEM-F200, JEOL, Japan) was conducted at an operating voltage of 200 kV. The crystallographic phases of the materials were identified by means of X-ray diffraction (XRD, Rigaku-2038, Japan). Pore structure analysis was carried out by measuring N_2 physisorption isotherms at 77 K on a surface area analyzer (ASAP 2460, Micromeritics, USA). The specific surface area was subsequently derived using the Brunauer–Emmett–Teller (BET) model, while the pore size distribution was evaluated *via* the Barrett–Joyner–Halenda (BJH) method. Furthermore, the graphitic nature and defect structures were probed by Raman spectroscopy (LabRAM HR Evolution, Horiba, Japan) with a 532 nm excitation laser. The elemental composition and chemical valence states were investigated by X-ray photoelectron spectroscopy (XPS, K-Alpha, Thermo Scientific, USA), utilizing monochromatic Al-Kα radiation as the excitation source.

In addition to structural characterization, the catalytic reaction products during the oxygen reduction reaction were quantitatively analyzed using rotating ring-disk electrode (RRDE) measurements. The disk current corresponds to the oxygen reduction process, while the ring electrode detects peroxide species generated during the reaction. Based on the disk and ring currents, the electron transfer number and H_2O_2 yield were calculated to determine the dominant ORR reaction pathway.

2.5 Electrochemical measurements

The electrocatalytic properties of the prepared materials were evaluated using a CHI660E electrochemical workstation configured with a standard three-electrode system. A glassy carbon electrode (GCE, 5 mm diameter) modified with the catalyst served as the working electrode. This modified electrode was fabricated by initially dispersing 5 mg of the catalyst powder in a mixture comprising 800 μL of anhydrous ethanol and 30 μL of Nafion (5 wt%) under ultrasonic treatment to yield a uniform ink. Subsequently, an aliquot of 10 μL of this dispersion was deposited onto the GCE surface *via* drop-casting. For benchmarking, the ORR activity of the as-synthesized catalysts was contrasted against that of a commercial Pt/C (20 wt%) reference material (HiSPEC 3000, Alfa Aesar).

Before initiating ORR measurements, the electrolyte (0.1 M KOH) was purged with either high-purity O_2 or N_2 for a minimum of 30 min to achieve saturation. Cyclic voltammetry (CV) profiles were acquired at a sweep rate of 50 mV s^{-1}, whereas linear sweep voltammetry (LSV) was performed at a slower rate of 5 mV s^{-1} to assess the ORR activity. The diffusion-limited current density was determined at a potential of 0.2 V *versus* the reversible hydrogen electrode (RHE). For kinetic analysis, rotating disk electrode (RDE) and RRDE experiments were carried out in O_2-saturated 0.1 M KOH at a scan rate of 10 mV s^{-1}. All potentials, originally measured

against an Ag/AgCl reference electrode, were converted to the RHE scale using the following relationship (eqn (1)).

$$E_{RHE} = E_{Ag/AgCl} + 0.197 + 0.0591pH \quad (1)$$

The formation of peroxide intermediates during ORR was quantified using the RRDE system. The disk electrode was used to drive the oxygen reduction reaction, while the platinum ring electrode was maintained at 1.20 V *vs.* RHE to oxidize the generated peroxide species. The peroxide yield (H_2O_2%) and the electron transfer number (n) were calculated from the disk and ring currents according to standard RRDE equations (eqn (2)). The measurements were conducted in O_2-saturated 0.1 M KOH electrolyte at a rotation speed of 1600 rpm and a scan rate of 10 mV s^{-1}. The H_2O_2 yield represents the fraction of oxygen molecules reduced through the two-electron pathway relative to the total oxygen reduction process. A lower H_2O_2 yield indicates a higher selectivity toward the desired four-electron pathway that converts O_2 directly into OH^-.

$$n = 4I_d(I_d + I_r/N) \quad (2)$$

Herein, I_d signifies the faradaic current at the disk electrode, I_r denotes the current at the ring electrode, and N refers to the collection efficiency of the ring, which was experimentally calibrated to be 0.37.

The oxygen evolution reaction (OER) activity was investigated *via* LSV in an O_2-saturated 1.0 M KOH solution at a scan rate of 5 mV s^{-1}, utilizing an identical catalyst loading to that employed in the ORR studies. To mitigate the influence of uncompensated resistance, all reported polarization curves were subjected to 95% *iR* correction. The operational durability of the as-synthesized materials was assessed by recording LSV profiles before and after subjecting the electrodes to 2000 successive potential cycles.

3 Results and discussion

3.1 Structural characterization and analysis

XRD was employed to probe the crystalline phase composition and structural attributes of the fabricated samples, with the resulting patterns presented in Fig. 1. Inspection of the diffractograms reveals that all three specimens (NiFe@CNT, Ni@CNT, and FeZn@CNT) share a common diffraction feature centered at $2\theta = 26.0°$. This peak is assigned to the (101) crystallographic plane of graphitic carbon, a characteristic signature of both carbon nanotubes and graphitic carbon matrices. For NiFe@CNT, the peaks at $2\theta = 44.5°$ and 51.8° are typical characteristic peaks of the NiFe alloy, indicating the formation of bimetallic alloy active sites during pyrolysis. For Ni@CNT, the characteristic peaks at $2\theta = 44.5°$ and 51.8° correspond to the (111) and (200) crystal planes of metallic Ni, respectively, revealing that Ni existed completely in the metallic state after pyrolysis and was uniformly anchored on the CNT support. No peaks related to nickel oxide or nickel carbide were detected in Ni@CNT, indicating that the intrinsic metallic activity of Ni was preserved. Notably, the atomic radius of Fe is very close to that

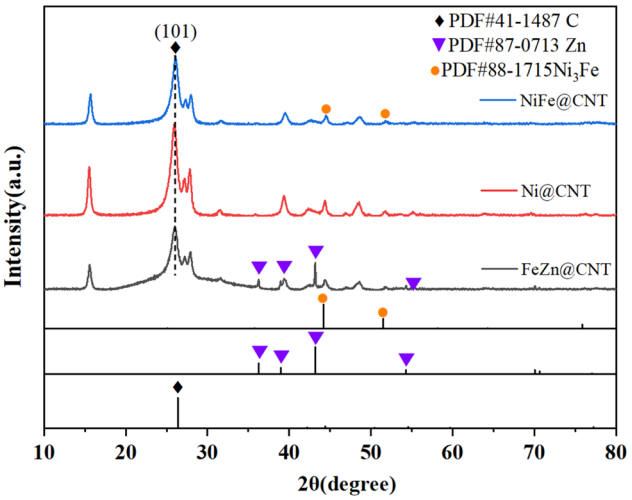

Fig. 1 XRD spectra of NiFe@CNT, Ni@CNT and ZnFe@CNT.

of Ni (Fe: ~126 pm; Ni: ~124 pm), which leads to highly similar diffraction patterns in XRD analysis, particularly for the characteristic alloy peaks observed in Fig. 1. For FeZn@CNT, the peaks at $2\theta = 36.3°$, 39.4°, 43.2°, and 54.3° correspond to the characteristic peaks of metallic Zn. Furthermore, no characteristic peaks assigned to Zn–Fe alloy were observed, demonstrating that Zn did not form a stable alloy phase with Fe. It should be noted that weak peaks corresponding to Fe_3O_4 ($2\theta = 30.1°$, 35.5°) and NiO ($2\theta = 37.2°$) appeared in all three XRD patterns, which can be attributed to slight oxidation of a small fraction of metals during pyrolysis and are regarded as normal.

To elucidate the elemental composition of the three samples, the chemical valence states of the constituent metal elements, and their interactions with the carbon support, XPS measurements were carried out, as shown in Fig. 2, S1 and S2 (SI). The survey spectra reveal that NiFe@CNT contains C, N, Ni, Fe, and O; Ni@CNT consists of C, N, Ni, and O; while FeZn@CNT is composed of C, N, Zn, Fe, and O. For all three samples, the high-resolution C 1s spectra can be deconvoluted into five components, corresponding to COOH, C═O, C–O, C–C, and C–H species. Among them, the relative contribution of the C–C component follows the order NiFe@CNT > Ni@CNT > FeZn@CNT, indicating that the carbon phase in NiFe@CNT exhibits a higher degree of graphitization than those in Ni@CNT and FeZn@CNT.[51] For NiFe@CNT (Fig. 2), the high-resolution Ni 2p spectrum exhibits characteristic peaks at 856 and 867 eV, accompanied by satellite peaks at approximately 862 and 872 eV associated with Ni^{2+}, as well as a distinct peak at 852 eV attributable to Ni^0. These features are characteristic of a NiFe alloy with a small amount of surface-oxidized Ni. In the high-resolution Fe 2p spectrum, the deconvoluted peaks at 712 and 727 eV correspond to Fe^{2+}, those at 716 and 722 eV are assigned to Fe^{3+}, and the peak at 706 eV is attributed to Fe^0. These results indicate that, in NiFe@CNT, Ni exists in both metallic and divalent states, while Fe is present in metallic, divalent, and trivalent forms. For Ni@CNT (Fig. S1), the Ni 2p spectrum displays a typical metallic Ni^0 peak at around 852 eV,

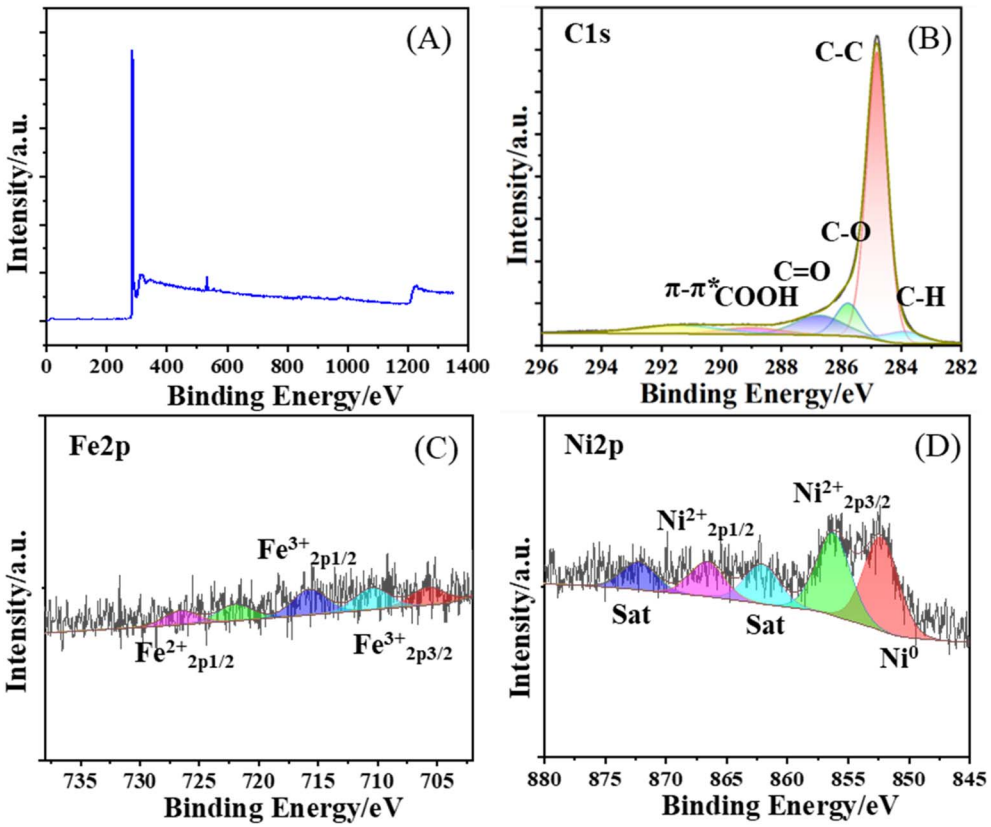

Fig. 2 XPS spectra of NiFe@CNT. (A) General scan, (B) C 1s, (C) Fe 2p, (D) Ni 2p.

together with Ni^{2+} features and their corresponding satellite peaks at higher binding energies, suggesting the coexistence of metallic and divalent nickel species in the material. In the case of ZnFe@CNT (Fig. S2), the Fe 2p spectrum suggests that Fe is mainly present in a mixed valence state of Fe^{2+} and Fe^{3+}. In addition, a weak Fe^0 signal is detected, implying that a small fraction of iron exists in the metallic state. The Zn 2p spectrum shows characteristic peaks at approximately 1022 and 1045 eV, which can be assigned to Zn^{2+}, indicating that zinc is present in the divalent state. This observation is consistent with and complementary to the results obtained from XRD analysis.

To evaluate the specific surface area, pore size distribution, and their potential influence on the electrocatalytic performance, BET measurements were conducted on the three samples, with the results presented in Fig. 3, S3 and S4. It was found that the pore size distributions and adsorption–desorption isotherms of the three samples were remarkably similar, indicating that modification with different metal elements does not affect the fundamental framework structure of the material. According to the IUPAC classification, the N_2 adsorption–desorption isotherms of all three tested samples at 77 K exhibited type IV isotherms with H4-type hysteresis loops, suggesting the presence of abundant mesopores (2–50 nm).

The influence of metal modification on textural properties was investigated through BET surface area analysis, with the results compiled in Fig. 3, S3 and S4. Inspection of the data revealed that all three samples share virtually identical pore size distributions and adsorption–desorption characteristics, indicating that the core framework remains intact regardless of the metal species introduced. Further analysis of the N_2 sorption isotherms measured at 77 K showed that each sample conforms to the type IV isotherm with an H4-type hysteresis loop according to IUPAC standards. This behavior is characteristic of materials containing extensive mesoporosity, specifically pores ranging from 2 to 50 nm in diameter. These mesopores are attributed to the interstitial pores within the CNT network and the superimposed microporous/mesoporous structures generated during the pyrolysis process, which aligns with the pore structure characteristics desirable for electrocatalytic materials. Application of the Brunauer–Emmett–Teller (BET) theory to the nitrogen sorption data yielded specific surface areas of 51 m^2 g^{-1} for NiFe@CNT, 50 m^2 g^{-1} for Ni@CNT, and 56 m^2 g^{-1} for ZnFe@CNT, considering the experimental uncertainty of BET measurements. Further analysis employing the Barrett–Joyner–Halenda (BJH) method coupled with the *t*-plot approach indicated that the pore size distributions for all three materials are predominantly situated within the mesoporous domain, specifically ranging from 2 to 50 nm, with a high degree of uniformity. Such well-defined porous characteristics are expected to enhance electrolyte permeation and promote the accessibility of active species to catalytic sites.

The surface morphology, growth state of CNTs, and overall morphological uniformity of the samples were examined using SEM, with the results presented in Fig. 4. It can be observed that

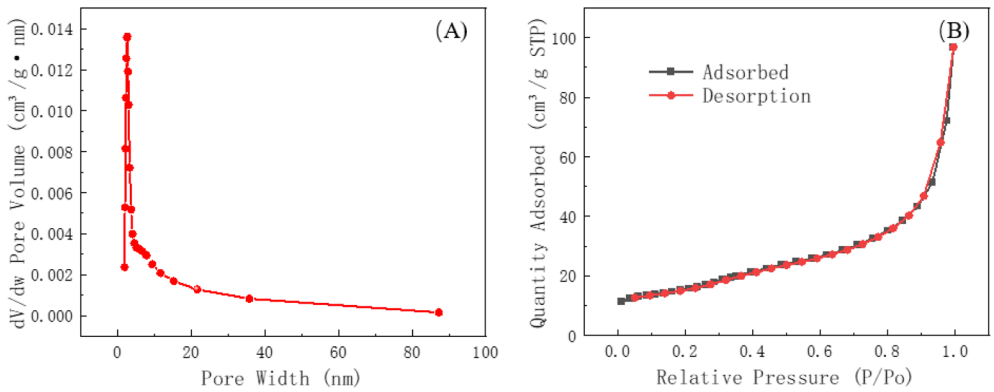

Fig. 3 N_2 adsorption/desorption isotherm (A) and pore size distribution (B) of NiFe@CNT.

all the samples exhibit a three-dimensional network structure composed of numerous intertwined one-dimensional CNTs. The CNTs are entangled and interwoven with each other, forming a continuous conductive framework. No obvious bulk aggregates or dense agglomerations are observed, indicating a relatively uniform overall morphology. Furthermore, the complete tubular structure of the CNTs and their relatively uniform diameter distribution can be clearly discerned. The individual CNTs exhibit considerable length and a high growth density, suggesting that the high-temperature pyrolysis process did not compromise the fundamental structure of the CNTs. Although the overall morphology of Ni@CNT and ZnFe@CNT (Fig. 4B and C) appears similar due to the presence of a carbon nanotube network, closer inspection reveals noticeable differences. In Ni@CNT, metallic Ni nanoparticles are relatively uniformly distributed along the CNT surfaces, while in ZnFe@CNT small aggregated particles are occasionally observed at CNT junctions, which may correspond to Zn-containing phases. These differences arise from the distinct metal species involved in the MOF precursor and their different behaviors during the pyrolysis process. Moreover, the elemental composition of the catalysts was further quantified using energy-dispersive X-ray spectroscopy (EDS). The results indicate that the NiFe@CNT composite contains approximately 3.2 wt% Ni and 2.8 wt% Fe, while ZnFe@CNT contains 3.5 wt% Zn and 2.6 wt% Fe, which is consistent with the results of XPS. These results confirm the successful incorporation of bimetallic species into the carbon matrix and support the formation of catalytically active sites.

To further verify the internal structure of the CNTs at the nanoscale, the fine microstructure of the samples was examined using TEM, with the results presented in Fig. 5. It can be observed that the samples exhibit a network structure formed by entangled and cross-linked carbon nanotubes. The CNTs are tightly interconnected, constructing a continuous three-dimensional conductive framework, with no obvious bulk

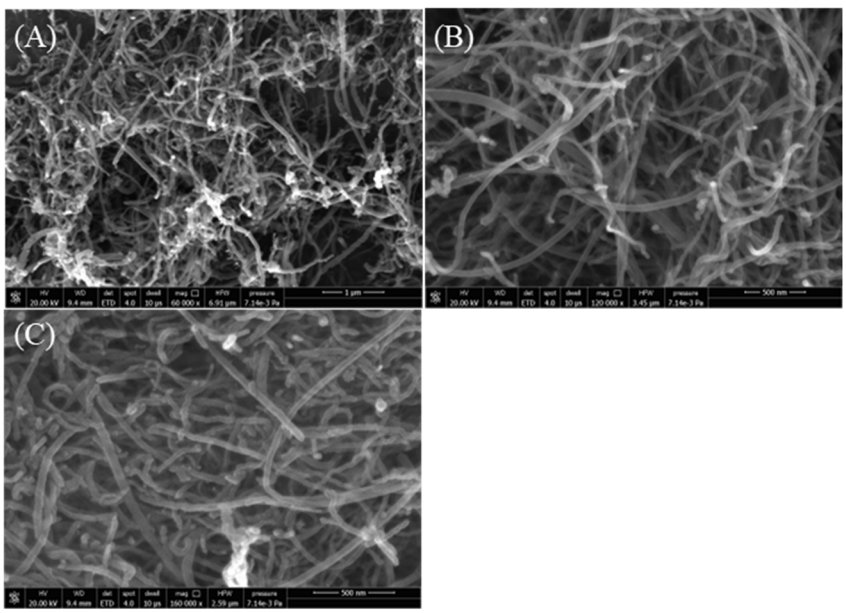

Fig. 4 SEM image of NiFe@CNT (A), Ni@CNT(B) and ZnFe@CNT (C).

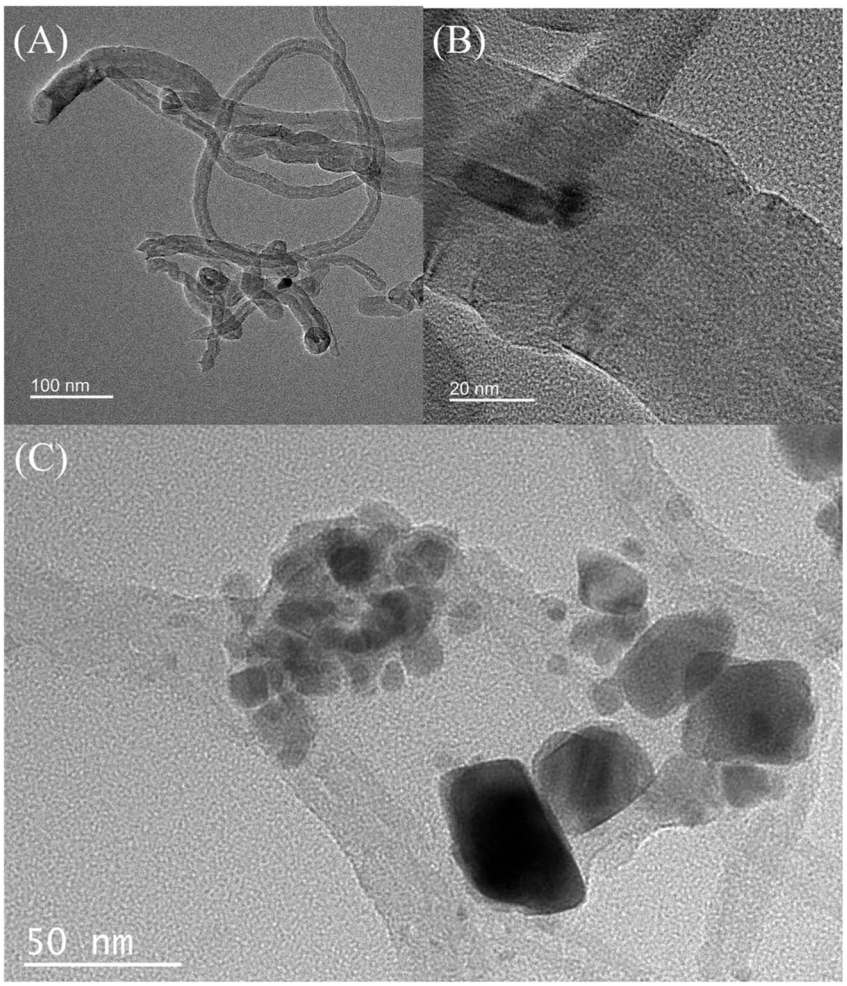

Fig. 5 TEM image of NiFe@CNT (A), Ni@CNT (B) and ZnFe@CNT (C).

agglomerations detected. Furthermore, closer inspection of the CNT wall structure reveals a relatively uniform diameter distribution, with CNT diameters measuring approximately 40–50 nm. The tube walls are intact and continuous, showing no significant collapse or fracture, indicating that the high-temperature pyrolysis process did not compromise the fundamental structure of the CNTs.

To probe the structural features of the carbon matrix, particularly regarding defects and graphitic ordering, Raman analysis was conducted on the as-prepared samples (Fig. 6). Inspection of the spectra revealed that each sample exhibits a distinct D-band at ~1350 cm^{-1} and a G-band at ~1580 cm^{-1} within the 500–2000 cm^{-1} region. The D-band is attributed to defective sites and amorphous carbon derived from sp^3-hybridized configurations, while the G-band corresponds to the characteristic stretching mode of sp^2-hybridized carbon in graphitic lattices. The relative intensity ratios (I_D/I_G) were subsequently determined to be 0.39, 0.43, and 0.51 for NiFe@CNT, Ni@CNT, and FeZn@CNT, respectively, reflecting variations in their defect densities and graphitization levels. The lower I_D/I_G value observed for NiFe@CNT indicates a higher degree of graphitization and fewer structural defects, which is

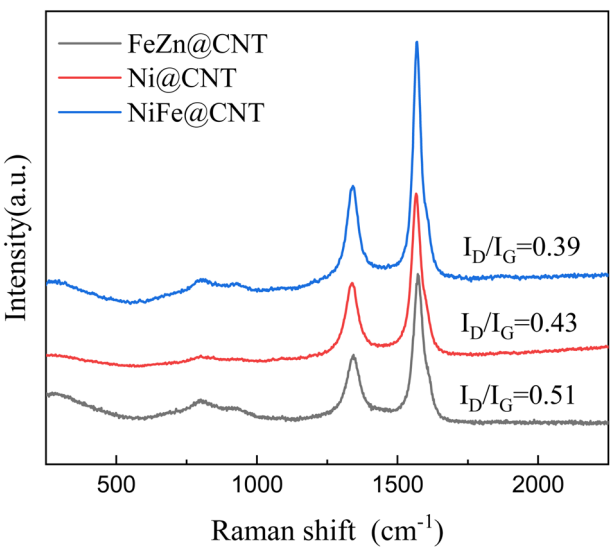

Fig. 6 Raman spectroscopy of NiFe@CNT, Ni@CNT and ZnFe@CNT.

conducive to enhanced electron transport and improved electrocatalytic performance.[52,53]

3.2 Electrochemical properties

The fundamental ORR activity of the materials was assessed *via* CV measurements, with the results shown in Fig. 7. For all three materials, no obvious reduction peaks were observed in the N_2-saturated electrolyte, whereas well-defined reduction peaks appeared in the O_2-saturated electrolyte, indicating that all three materials possess certain ORR activity. Under O_2-saturated electrolyte conditions, the reduction peak potentials for NiFe@CNT, Ni@CNT, and ZnFe@CNT were 0.84, 0.79, and 0.73 V, respectively. Furthermore, based on the intensity and definition of the reduction peaks, NiFe@CNT exhibited the most prominent performance, followed by Ni@CNT, while ZnFe@CNT showed relatively weaker features. Based on the CV results, NiFe@CNT exhibits the highest ORR activity among the three catalysts. The comparison between NiFe@CNT and Ni@CNT highlights the crucial role of Fe incorporation in enhancing catalytic activity, while the comparison between NiFe@CNT and ZnFe@CNT further demonstrates the importance of the Ni–Fe bimetallic synergistic effect.

It is generally accepted that for electrocatalytic materials, a more positive onset potential (E_{onset}) and half-wave potential ($E_{1/2}$), along with a larger absolute value of the limiting current density (J_L) in LSV curves, indicate superior ORR electrocatalytic performance.[54,55] Here, using commercial Pt/C as a benchmark, the electrocatalytic performance of the three materials was further analyzed *via* LSV measurements, with the results presented in Fig. 8A. E_{onset} for NiFe@CNT, Ni@CNT, and ZnFe@CNT were 0.932 V, 0.914 V, and 0.909 V, respectively; their $E_{1/2}$ were 0.846 V, 0.791 V, and 0.718 V, respectively; and their J_L were −5.14 mA cm^{-2}, −4.76 mA cm^{-2}, and −4.42 mA cm^{-2}, respectively. Therefore, based on the LSV curves, the ORR electrocatalytic performance of the three materials follows the order, namely NiFe@CNT > Ni@CNT > ZnFe@CNT. Furthermore, the ORR performance of NiFe@CNT is even comparable to that of commercial Pt/C (E_{onset} = 0.974 V, $E_{1/2}$ = 0.823 V, J_L = 5.72 mA cm^{-2}).

To elucidate the kinetic parameters governing the oxygen reduction reaction, Tafel plots were constructed from the LSV data, as displayed in Fig. 8B. The extracted Tafel slopes for NiFe@CNT, Ni@CNT, and ZnFe@CNT were found to be 65.73, 93.46, and 112.35 mV dec^{-1}, respectively. It is a widely accepted tenet in electrocatalysis that a steeper Tafel slope (*i.e.*, a larger numerical value) is associated with slower reaction kinetics, whereas a shallower slope reflects more rapid electron transfer during the rate-determining step.[56,57] Consequently, the minimal Tafel slope exhibited by NiFe@CNT underscores its kinetic superiority, a conclusion that mirrors the performance hierarchy established through LSV analysis.

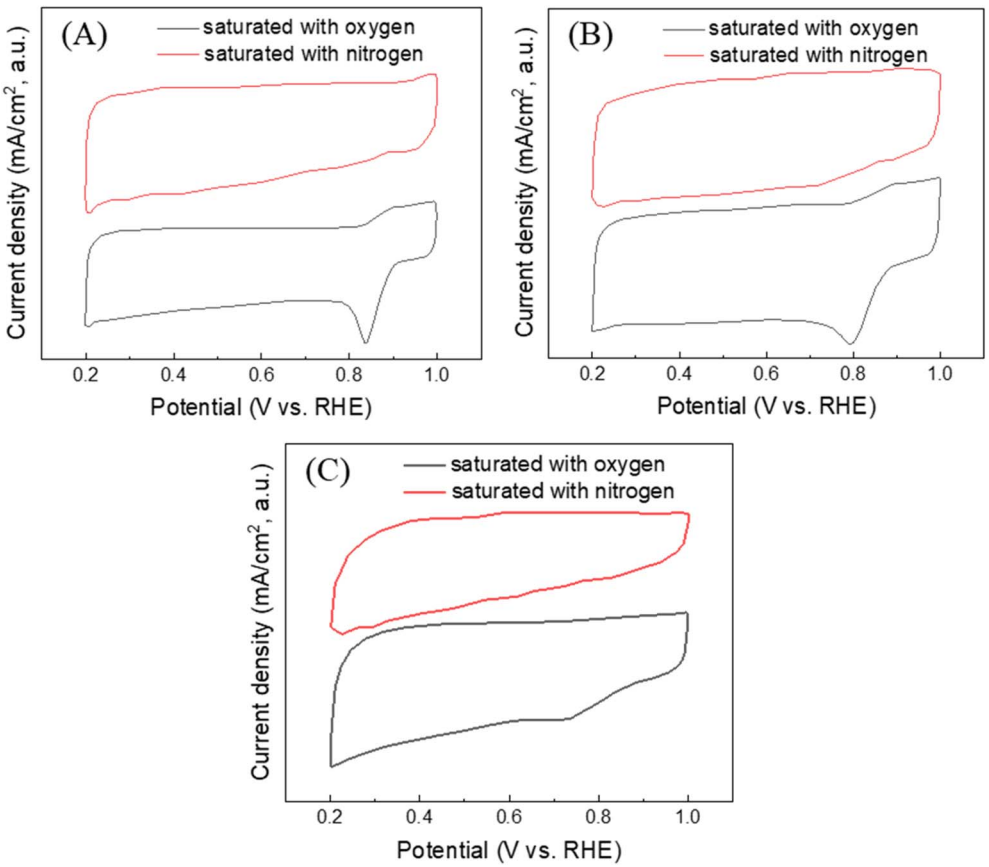

Fig. 7 CV curves of NiFe@CNT (A), Ni@CNT (B) and ZnFe@CNT (C) in 0.1 M KOH electrolyte saturated with N_2 and O_2.

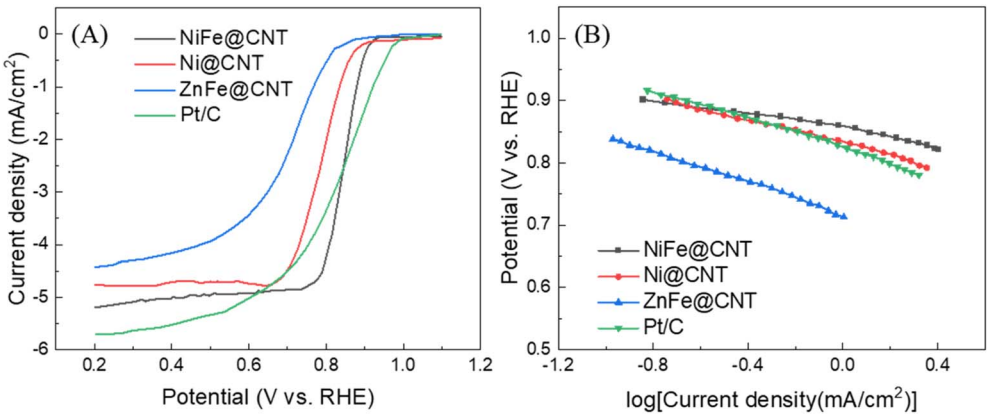

Fig. 8 (A) LSV curves of NiFe@CNT, Ni@CNT, ZnFe@CNT, and Pt/C in O_2-saturated 0.1 M KOH; (B) Tafel slopes derived from the LSV curves.

In addition to kinetic parameters, the efficiency of charge transfer across the electrode/electrolyte interface plays a pivotal role in determining overall catalytic activity. Electrochemical impedance spectroscopy (EIS) was therefore employed to investigate this aspect, with the resulting Nyquist plots presented in Fig. S5. The charge transfer resistance (R_{ct}), which correlates inversely with the diameter of the semicircular arc in the high-frequency region, is a key metric for assessing interfacial electron transport.[58–60] Examination of the impedance spectra revealed a distinct progression in arc diameters, increasing in the order NiFe@CNT < Ni@CNT < ZnFe@CNT. This sequence unequivocally demonstrates that NiFe@CNT possesses the lowest charge transfer resistance and thus the most efficient electron transfer kinetics, providing compelling corroboration of its enhanced electrocatalytic performance relative to Ni@CNT and ZnFe@CNT.

Based on the comprehensive results of the CV, LSV, Tafel slopes, and EIS tests described above, NiFe@CNT exhibited the optimal ORR electrocatalytic performance. Therefore, NiFe@CNT was selected for further LSV polarization curve measurements at different rotation speeds to evaluate its stability, with the results shown in Fig. S6. At various rotation speeds, E_{onset} of this material remained stable at approximately 0.932 V, indicating good electrochemical stability. Corresponding to rotation speeds ranging from 400 rpm to 1600 rpm, its $E_{1/2}$ were 0.869 V, 0.861 V, 0.854 V, 0.849 V, and 0.844 V, respectively. Although the rotation speed increased by 1200 rpm within the range of 400 rpm to 1600 rpm, the $E_{1/2}$ exhibited a change of only 0.025 V. This result falls within a reasonable margin of error, further demonstrating the material's good stability. Regarding the limiting current density, a clear increase was observed with increasing rotation speed, indicating a progressive enhancement in the electrocatalytic ORR performance.

The electron transfer number and H_2O_2 yield were additionally determined using the RRDE technique. As shown in Fig. 9A, the H_2O_2 yield of NiFe@CNT was 9.5%, which is lower than those of Co@CNT (31.3%) and ZnFe@CNT (57.6%). The low H_2O_2 yield of CoFe@CNT confirms that its ORR process proceeds *via* a four-electron pathway. According to Fig. 9B, the electron transfer numbers for the NiFe@CNT, Ni@CNT, and ZnFe@CNT catalysts were 3.9, 3.5, and 2.9, respectively, confirming a four-electron pathway for the NiFe@CNT catalyst. This result indicates that NiFe@CNT exhibits a desirable four-electron transfer mechanism under alkaline conditions, similar to that observed for the commercial Pt/C catalyst. This favorable four-electron process effectively suppresses H_2O_2 production, thereby facilitating the conversion of O_2 to H_2O during the ORR.

The operational robustness of NiFe@CNT was scrutinized through chronoamperometric (*i*–*t*) measurements performed at a constant applied potential of 0.8 V *vs.* RHE, as illustrated in Fig. S7. Impressively, the NiFe@CNT electrode demonstrated minimal current attenuation, sustaining 93.4% of its initial current density after continuous operation for more than 20 000 seconds. By contrast, the state-of-the-art Pt/C catalyst, tested under identical conditions, exhibited a more substantial deterioration, retaining only 74.5% of its original current. This stark disparity unequivocally attests to the superior electrochemical durability of NiFe@CNT.

In addition to ORR activity, the OER performance was systematically evaluated to confirm the bifunctional electrocatalytic potential of the materials. LSV was employed to acquire polarization curves in an O_2-saturated 1.0 M KOH electrolyte, with RuO_2 serving as a benchmark for comparison (Fig. 10A). The onset potentials, marking the commencement of the OER, were measured as 1.476 V for NiFe@CNT, 1.499 V for Ni@CNT, 1.532 V for ZnFe@CNT, and 1.484 V for RuO_2. More importantly, the potentials required to achieve a current density of 10 mA cm^{-2}—a key metric for comparing OER catalysts—were found to be 1.514 V for NiFe@CNT, 1.636 V for Ni@CNT, 1.751 V for ZnFe@CNT, and 1.578 V for RuO_2. According to well-established criteria in electrocatalysis, lower onset potentials and reduced overpotentials at 10 mA cm^{-2} are indicative of enhanced OER kinetics. Thus, the data conclusively demonstrate that NiFe@CNT possesses superior OER catalytic activity relative to both Ni@CNT and ZnFe@CNT.

To further analyze the reaction kinetics during OER, the Tafel slopes of each electrocatalytic material were fitted, with the results presented in Fig. 10B. It can be observed that the

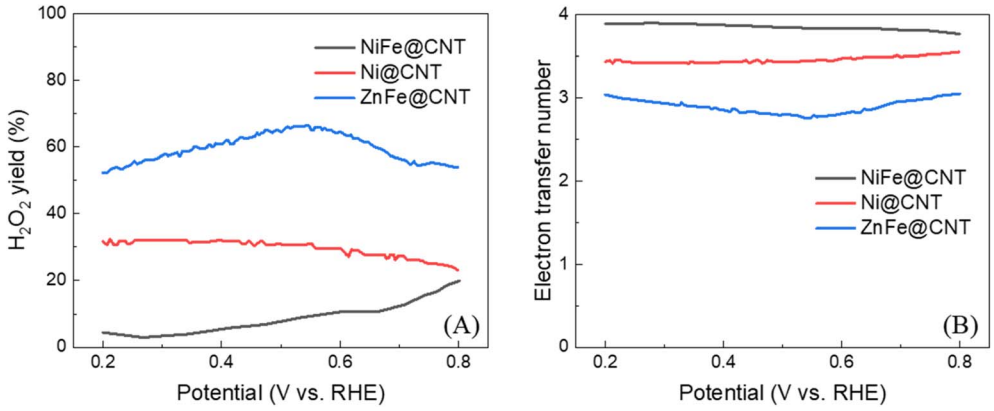

Fig. 9 H_2O_2 yield (A) and electron transfer number (B) of NiFe@CNT, Ni@CNT and ZnFe@CNT during ORR process.

Tafel slopes corresponding to the NiFe@CNT, Ni@CNT, ZnFe@CNT, and RuO_2 electrodes are 93.48 mV dec^{-1}, 109.25 mV dec^{-1}, 127.16 mV dec^{-1}, and 99.21 mV dec^{-1}, respectively. It is generally believed that a smaller Tafel slope indicates more favorable OER kinetics. Therefore, the OER performance of NiFe@CNT is superior to that of Ni@CNT and ZnFe@CNT, which is consistent with the findings from the LSV during OER.

3.3 Mechanism of NiFe@CNT' enhanced bifunctional catalytic performance

ORR and OER are core half-reactions in energy conversion devices such as fuel cells and water electrolyzers. Their sluggish reaction kinetics necessitate efficient bifunctional catalysts to lower the reaction energy barriers. The aforementioned results demonstrate that the ORR/OER bifunctional catalytic activity of NiFe@CNT is significantly superior to that of Ni@CNT and ZnFe@CNT. Herein, the intrinsic mechanism underlying the excellent bifunctional catalytic performance of NiFe@CNT can be elucidated from phase structure, microscopic morphology, electronic states, chemical bonding, and active site characteristics.

XRD characterization (Fig. 1) clarified the differences in the crystalline phase structures of NiFe@CNT, Ni@CNT, and ZnFe@CNT, as the phase characteristics directly determine the intrinsic activity of the catalytic sites. After pyrolysis of NiFe-MOF, Ni and Fe ions are reduced to form an active NiFe alloy phase. Compared to the single Ni element in Ni@CNT and the single Fe element along with ZnO impurity phases in ZnFe@CNT, the NiFe alloy exhibits significantly enhanced intrinsic ORR/OER catalytic activity due to the bimetallic electronic coupling effect. Simultaneously, its ultra-fine dispersion state further increases the density of active sites, and the absence of interfering inactive phases allows the active sites to function optimally. In contrast, Ni@CNT possesses only single Ni active sites, and grain agglomeration leads to insufficient exposure of these sites. ZnFe@CNT contains inactive ZnO impurity phases, and Fe species may undergo agglomeration, both of which prevent the formation of an efficient bifunctional catalytically active phase.

SEM and TEM images (Fig. 4 and 5) reveal that the CNTs in NiFe@CNT maintain an intact interwoven tubular structure without significant agglomeration. The three-dimensional porous network morphology of NiFe@CNT enables synergistic

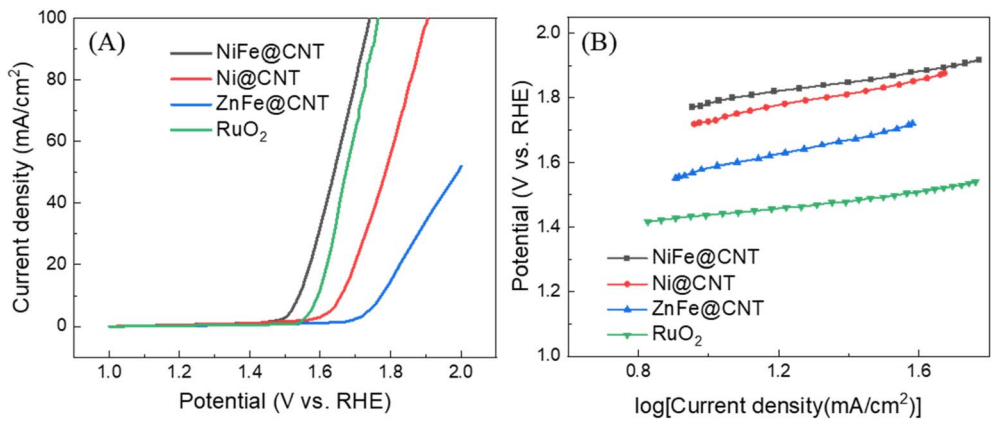

Fig. 10 (A) LSV polarization curves of NiFe@CNT, Ni@CNT, ZnFe@CNT and RuO_2 for the OER in 1 M KOH solution; (B) Tafel slopes derived from the OER curves.

optimization of active sites, mass transfer, and electron conduction. On the one hand, the high specific surface area and uniform pore structure substantially increase the exposure of active sites while accelerating the diffusion rate of O_2 and H_2O molecules in the electrolyte. This reduces the mass transfer resistance for ORR/OER, facilitating rapid access of reactants to the active sites and timely removal of products. On the other hand, the intact CNT tubular structure, combined with the uniform dispersion of the NiFe alloy, constructs continuous electron transport channels, minimizing charge loss during electron transfer and enhancing electron conduction efficiency.

The Raman spectra of the three electrocatalysts (Fig. 6) indicate that NiFe@CNT achieves a dual enhancement in both electron conduction and active site activity. The low I_D/I_G ratio of NiFe@CNT, corresponding to a higher degree of graphitization and moderate defect density within the CNTs, constructs efficient and continuous electron transport channels. This significantly improves electron conduction efficiency, overcoming the electron transport limitations observed in Ni@CNT and ZnFe@CNT, and provides sufficient electron supply for ORR/OER reactions. Furthermore, the moderate defect sites enable efficient adsorption and activation of O_2 and H_2O molecules. Simultaneously, the excellent structural stability arising from the high graphitization degree, combined with the robust interfacial integration between the NiFe bimetallic species and the CNTs, enhances the long-term durability of the catalyst. Additionally, the synergistic effect of the NiFe bimetallic components underlying the low I_D/I_G ratio further strengthens the intrinsic catalytic activity of the active sites, leading to a synergistic improvement in ORR/OER bifunctional catalytic performance. In contrast, Ni@CNT and ZnFe@CNT exhibit higher I_D/I_G ratios, indicating insufficient graphitization and excessive defects within the CNTs. This results in low electron conduction efficiency and poor structural stability. Moreover, the absence of bimetallic synergy fails to enhance the active site activity. Consequently, their bifunctional catalytic performance is significantly inferior to that of NiFe@CNT. This mechanism also clarifies the regulatory role of the I_D/I_G ratio from Raman spectroscopy in governing the bifunctional catalytic performance of MOF-derived carbon-based bimetallic catalysts, providing a theoretical reference for performance optimization of analogous catalysts.

XPS characterization (Fig. 2, S1 and S2) revealed the chemical states, electronic distribution, and surface-active species content of each element in the three materials, elucidating the core reasons for the bifunctional catalytic advantages of NiFe@CNT from the perspectives of electronic state modulation and active species optimization. First, the electronic coupling effect of the NiFe bimetallic components significantly increases the content of high-valence Ni^{3+} (ORR active centers) and Fe^{3+} (OER active centers), while simultaneously modulating the electron cloud density of the metal ions. This lowers the reaction energy barriers for ORR/OER, achieving a synergistic enhancement in bifunctional catalytic activity. Secondly, the presence of abundant hydroxyl oxygen promotes the generation of $^{\bullet}OH$ species, thereby reinforcing indirect catalytic effects. Concurrently, oxygen-containing functional groups increase the number of O_2 adsorption sites, accelerating ORR reaction kinetics. Thirdly, the chemical bonding between the metals and the CNTs ensures efficient electron transfer, enabling a synergistic interaction between the active sites and the conductive channels, which further enhances catalytic efficiency. In contrast, Ni@CNT possesses only single Ni active sites with a low content of high-valence active centers. ZnFe@CNT also suffers from a low content of high-valence active centers and the presence of inactive impurity phases. Consequently, neither material achieves the optimization of electronic states and active species observed in NiFe@CNT, resulting in limited bifunctional catalytic activity.

Therefore, the fundamental reason why NiFe@CNT exhibits superior ORR/OER bifunctional catalytic performance lies in its synergistic enhancement across four dimensions, namely crystalline phase, structure, electronic state, and active sites, which is significantly superior to Ni@CNT and ZnFe@CNT. Compared to Ni@CNT, NiFe@CNT forms an active NiFe bimetallic alloy phase, overcoming the issues of single active sites and grain agglomeration. The bimetallic electronic coupling effect enhances the intrinsic activity of the active sites. Compared to ZnFe@CNT, NiFe@CNT avoids the formation of inactive ZnO impurity phases, achieving uniform dispersion of the bimetallic alloy while simultaneously improving electron conduction efficiency and increasing the content of active species.

4 Conclusions

In this work, a Ni-modified bimetallic MOF-derived carbon-based composite catalyst, NiFe@CNT, was successfully constructed using a two-dimensional metalloporphyrin-based Fe-MOF precursor *via* Ni introduction and a temperature-programmed pyrolysis strategy. Its bifunctional electrocatalytic performance and enhancement mechanism for ORR/OER were investigated. Through comparison with Ni@CNT and ZnFe@CNT, the crucial role of the NiFe bimetallic synergistic effect and structural advantages in enhancing catalytic performance was elucidated. XRD and XPS results confirmed the successful formation of the NiFe alloy and the coexistence of multiple valence states of Ni and Fe. Raman analysis revealed that NiFe@CNT possesses a higher degree of graphitization and superior carbon structural integrity. Electrochemical tests demonstrated that NiFe@CNT exhibits significantly superior ORR/OER bifunctional catalytic activity compared to Ni@CNT and ZnFe@CNT under alkaline conditions. During the ORR process, NiFe@CNT displayed a more positive onset potential (0.932 V) and half-wave potential (0.846 V), a smaller Tafel slope (65.73 mV dec^{-1}), and lower charge transfer impedance. RRDE measurements confirm that NiFe@CNT follows a four-electron ORR pathway with an electron transfer number close to 4. For the OER, the overpotential required to reach 10 mA cm^{-2} (1.514 V) was significantly lower than that of the reference samples, accompanied by superior reaction kinetics. Furthermore, long-term stability tests indicated that NiFe@CNT exhibits good electrochemical stability with minimal current decay during continuous operation. Additionally, the enhancement mechanism underlying the excellent ORR/OER bifunctional catalytic

performance of NiFe@CNT was elucidated by combining structural characterization with electrochemical testing.

Author contributions

Yunyang Wu was responsible for writing – original draft, data curation, formal analysis, resources, software, funding acquisition, validation, writing – review and editing.

Conflicts of interest

I declare that there are no competing financial interests or personal relationships that could have appeared to influence the work reported in this paper.

Data availability

The author declares that the data supporting the findings of this study are available within the paper and its supplementary information (SI). Should any raw data files be needed in another format they are available from the corresponding author upon reasonable request. Source data are provided with this paper. Supplementary information is available. See DOI: https://doi.org/10.1039/d6ra01624c.

Acknowledgements

This research did not receive any specific grant from funding agencies in the public, commercial, or not-for-profit sectors.

References

1 A. Aijaz, J. Masa, C. Roesler, *et al.*, Co@Co_3O_4 Encapsulated in Carbon Nanotube-Grafted Nitrogen-Doped Carbon Polyhedra as an Advanced Bifunctional Oxygen Electrode, *Angew. Chem., Int. Ed.*, 2016, **55**(12), 4087–4091.
2 J. Xu, C. Chen, Z. Han, *et al.*, Recent Advances in Oxygen Electrocatalysts Based on Perovskite Oxides, *Nanomaterials*, 2019, **9**(8), 1161.
3 Y. Zhu, W. Zhou and Z. Shao, Perovskite/Carbon Composites: Applications in Oxygen Electrocatalysis, *Small*, 2017, **13**(12), 1603793.
4 A. Ali, J. M. Moradian, A. Naveed, *et al.*, Progress in cathode materials for rechargeable Zinc-Ion batteries: from inorganic and organic systems to hybrid frameworks and biomass-derived innovations, *Prog. Mater. Sci.*, 2025, 101543.
5 Y. Jiao, K. Xu, H. N. Xiao, *et al.*, Biomass-Derived Carbon Aerogels for ORR/OER Bifunctional Oxygen Electrodes, *Nanomaterials*, 2023, **13**(17), 2397.
6 J. X. Liu, Y. Wang, Y. T. Gu, *et al.*, Oxygen electrode catalysis in N-doped graphene: the role of nitrogen coordination and solvation effects, *Nanoscale*, 2024, **16**(47), 21937–21946.
7 A. Zitolo, N. Ranjbar-Sahraie, T. Mineva, *et al.*, Identification of catalytic sites in cobalt-nitrogen-carbon materials for the oxygen reduction reaction, *Nat. Commun.*, 2017, **8**(1), 957.
8 C. L. Mcbean, H. Q. Liu, M. E. Scofield, *et al.*, Generalizable, Electroless, Template-Assisted Synthesis and Electrocatalytic Mechanistic Understanding of Perovskite $LaNiO_3$ Nanorods as Viable, Supportless Oxygen Evolution Reaction Catalysts in Alkaline Media, *ACS Appl. Mater. Interfaces*, 2017, **9**(29), 24634–24648.
9 S. Chen, L. Zhang, Z. Liu, *et al.*, Constructing Stable Bifunctional Electrocatalyst of Co–$Co_2Nb_5O_{14}$ with Reversible Interface Reconstitution Ability for Sustainable Zn-Air Batteries, *Adv. Sci.*, 2025, **12**(17), 2413796.
10 L. Wang, Z. Xu, T. Peng, *et al.*, Bifunctional Single-Atom Cobalt Electrocatalysts with Dense Active Sites Prepared via a Silica Xerogel Strategy for Rechargeable Zinc-Air Batteries, *Nanomaterials*, 2022, **12**(3), 381.
11 H. F. Wang, L. Y. Chen, H. Pang, *et al.*, MOF-derived electrocatalysts for oxygen reduction, oxygen evolution and hydrogen evolution reactions, *Chem. Soc. Rev.*, 2020, **49**(5), 1414–1448.
12 L. Tang, M. Cai, M. Zhang, *et al.*, LDH-assisted growth of FeCo bimetal-MOF nanorods for electrocatalytic oxygen evolution, *RSC Adv.*, 2022, **12**(38), 25112–25117.
13 Q. Ren, H. Wang, X.-F. Lu, *et al.*, Recent Progress on MOF-Derived Heteroatom-Doped Carbon-Based Electrocatalysts for Oxygen Reduction Reaction, *Adv. Sci.*, 2018, **5**(3), 1700515.
14 L. Li, Y. J. Chen, H. R. Xing, *et al.*, Single-atom Fe-N5 catalyst for high-performance zinc-air batteries, *Nano Res.*, 2022, **15**(9), 8056–8064.
15 Y. J. Yuan, R. Zhang, D. Pan, *et al.*, Advances in atomically dispersed metal-nitrogen-carbon catalysts derived from metal-organic frameworks for zinc-air batteries, *Coord. Chem. Rev.*, 2025, **545**, 217050.
16 Q. H. Huang, A. Zeb, Z. H. Xu, *et al.*, Fe-based metal-organic frameworks and their derivatives for electrochemical energy conversion and storage, *Coord. Chem. Rev.*, 2023, **494**, 215335.
17 S. S. Zheng, X. R. Li, B. Y. Yan, *et al.*, Transition-Metal (Fe, Co, Ni) Based Metal-Organic Frameworks for Electrochemical Energy Storage, *Adv. Energy Mater.*, 2017, **7**(18), 1602733.
18 Z. B. Liang, C. Qu, W. H. Guo, *et al.*, Pristine Metal-Organic Frameworks and their Composites for Energy Storage and Conversion, *Adv. Mater.*, 2018, **30**(37), 1702891.
19 D. Liu, J. W. Wan, G. S. Pang, *et al.*, Hollow Metal-Organic-Framework Micro/Nanostructures and their Derivatives: Emerging Multifunctional Materials, *Adv. Mater.*, 2019, **31**(38), 1803291.
20 J. W. Chang, Q. Zhang, J. K. Yu, *et al.*, A Fe Single Atom Seed-Mediated Strategy Toward Fe_3C/Fe-N-C Catalysts with Outstanding Bifunctional ORR/OER Activities, *Adv. Sci.*, 2023, **10**(22), 2301656.
21 S. N. U. Z. Haider, W. A. Qureshi, R. N. Ali, *et al.*, Contemporary advances in photocatalytic CO_2 reduction using single-atom catalysts supported on carbon-based materials, *Adv. Colloid Interface Sci.*, 2024, **323**, 103068.
22 Y. Yu, Y. Wang, F. Yang, *et al.*, Meso/Microporous Single-Atom Catalysts Featuring Curved Fe-N_4 Sites Boost the Oxygen Reduction Reaction Activity, *Angew. Chem., Int. Ed.*, 2025, **137**(3), e202415691.

23 Y. Wang, J. H. Wang, X. T. Feng, *et al.*, Synergistic Fe-Ni dual-atom sites on hollow carbon enabling high-performance rechargeable zinc-air batteries, *Chem. Sci.*, 2025, **17**(4), 2155–2163.
24 H. W. Zhang, M. Q. Zhao, H. R. Liu, *et al.*, Ultrastable FeCo Bifunctional Electrocatalyst on Se-Doped CNTs for Liquid and Flexible All-Solid-State Rechargeable Zn-Air Batteries, *Nano Lett.*, 2021, **21**(5), 2255–2264.
25 L. Chen, H. F. Wang, C. Li, *et al.*, Bimetallic metal–organic frameworks and their derivatives, *Chem. Sci.*, 2020, **11**(21), 5369–5403.
26 L. Hong, Q. Yang, R. Zhang, *et al.*, A Novel Strategy Synthesized Highly Specific Surface Area Bimetallic CoMn-MOFs as Electrode Materials for Supercapacitors, *J. Inorg. Organomet. Polym. Mater.*, 2025, **35**(10), 8391–8403.
27 S. S. Li, Y. Q. Gao, N. Li, *et al.*, Transition metal-based bimetallic MOFs and MOF-derived catalysts for electrochemical oxygen evolution reaction, *Energy Environ. Sci.*, 2021, **14**(4), 1897–1927.
28 Y. T. Zhou, R. Abazari, J. Chen, *et al.*, Bimetallic metal-organic frameworks and MOF-derived composites: Recent progress on electro- and photoelectrocatalytic applications, *Coord. Chem. Rev.*, 2022, **451**, 214264.
29 H. Wang, L. Yang, Y. N. Yang, *et al.*, Multifunctional bimetallic MOF engineering: Innovative synthesis and versatile applications in adsorption, catalysis, sensing, and energy, *Coord. Chem. Rev.*, 2026, **547**, 217114.
30 L. Yang, X. F. Zeng, W. C. Wang, *et al.*, Recent Progress in MOF-Derived, Heteroatom-Doped Porous Carbons as Highly Efficient Electrocatalysts for Oxygen Reduction Reaction in Fuel Cells, *Adv. Funct. Mater.*, 2018, **28**(7), 1704537.
31 Y. Yang, W. H. Ji, Y. T. Yin, *et al.*, Catalytic Modification of Porous Two-Dimensional Ni-MOFs on Portable Electrochemical Paper-Based Sensors for Glucose and Hydrogen Peroxide Detection, *Biosensors*, 2023, **13**(5), 508.
32 L. Yaqoob, T. Noor, N. Iqbal, *et al.*, Electrochemical synergies of Fe-Ni bimetallic MOF CNTs catalyst for OER in water splitting, *J. Alloys Compd.*, 2021, **850**, 156583.
33 C. Scheidler, J. Sobotta, W. Eisenreich, *et al.*, Unsaturated C3,5,7,9-Monocarboxylic Acids by Aqueous, One-Pot Carbon Fixation: Possible Relevance for the Origin of Life, *Sci. Rep.*, 2016, **6**(1), 27595.
34 Y. Li, L. Yang, X. L. Hao, *et al.*, Origin of Enhanced Oxygen Evolution in Restructured Metal-Organic Frameworks for Anion Exchange Membrane Water Electrolysis, *Angew. Chem., Int. Ed.*, 2025, **64**(1), e202413916.
35 G. Y. Yang, M. H. Fan, Q. Liang, *et al.*, Atomically Dispersed Fe_2 and Ni Sites for Efficient and Durable Oxygen Electrocatalysis, *Angew. Chem., Int. Ed.*, 2025, **64**(10), e202421168.
36 S. Tian, L. H. Chen, S. Wu, *et al.*, Application of asymmetric FeN_4-NiN_3O diatomic bifunctional catalysts with d-d coupling in zinc-air batteries, *Chem. Eng. J.*, 2025, **520**, 166120.
37 B. Song, K. Li, Y. Yin, *et al.*, Tuning Mixed Nickel Iron Phosphosulfide Nanosheet Electrocatalysts for Enhanced Hydrogen and Oxygen Evolution, *ACS Catal.*, 2017, **7**(12), 8549–8557.
38 Z. J. Zhu, H. J. Yin, Y. Wang, *et al.*, Coexisting Single-Atomic Fe and Ni Sites on Hierarchically Ordered Porous Carbon as a Highly Efficient ORR Electrocatalyst, *Adv. Mater.*, 2020, **32**(42), 2004670.
39 W. R. Cheng, X. Zhao, H. Su, *et al.*, Lattice-strained metal-organic-framework arrays for bifunctional oxygen electrocatalysis, *Nat. Energy*, 2019, **4**(2), 115–122.
40 A. Yu and Y. Yang, Atomically dispersed metal catalysts for oxygen reduction reaction: two-electron vs. four-electron pathways, *Angew. Chem.*, 2025, **137**(16), e202424161.
41 L. Zhang, S. Jiang, W. Ma, *et al.*, Oxygen reduction reaction on Pt-based electrocatalysts: Four-electron vs. two-electron pathway, *Chin. J. Catal.*, 2022, **43**(6), 1433–1443.
42 Z. Liang, H. Lei, H. Zheng, *et al.*, Selective two-electron and four-electron oxygen reduction reactions using Co-based electrocatalysts, *Chem. Soc. Rev.*, 2025, **54**(11), 5248–5291.
43 N. Yao, N. Luo, S. Jiang, *et al.*, Manipulated reaction route for oxyhydroxides toward top-performing water oxidation via e_g electron filling state, *Adv. Funct. Mater.*, 2024, **34**(40), 2405474.
44 I. Stassen, N. C. Burtch, A. A. Talin, *et al.*, An updated roadmap for the integration of metal-organic frameworks with electronic devices and chemical sensors, *Chem. Soc. Rev.*, 2017, **46**(11), 3185–3241.
45 D. W. Feng, T. Lei, M. R. Lukatskaya, *et al.*, Robust and conductive two-dimensional metal-organic frameworks with exceptionally high volumetric and areal capacitance, *Nat. Energy*, 2018, **3**(1), 30–36.
46 D. N. Xing, Y. Y. Wang, P. Zhou, *et al.*, Co_3(hexaiminotriphenylene)$_2$: A conductive two-dimensional π-d conjugated metal-organic framework for highly efficient oxygen evolution reaction, *Appl. Catal., B: Environ. Energy*, 2020, **278**, 119295.
47 J. J. Liu, X. Y. Song, T. Zhang, *et al.*, 2D Conductive Metal-Organic Frameworks: An Emerging Platform for Electrochemical Energy Storage, *Angew. Chem., Int. Ed.*, 2021, **60**(11), 5612–5624.
48 J. Z. Li, L. T. Lin, H. Q. Ai, *et al.*, A Hexaiminohexaazatrinaphthalene-Based 2D Conjugated Metal-organic Framework with Regulable Dual Metal Active Sites for Highly Efficient OER Activity, *Small*, 2026, **22**(1), e09720.
49 S. Liu, Y. Z. Qiu, Y. F. Liu, *et al.*, Recent advances in bimetallic metal-organic frameworks (BMOFs): synthesis, applications and challenges, *New J. Chem.*, 2022, **46**(29), 13818–13837.
50 S. Vignesh, K. Ahmad and T. H. Oh, Progress in Nickel MOF-Based Materials for Electrochemical Biosensor and Supercapacitor Applications, *Biosensors*, 2025, **15**(9), 560.
51 R. Shao, F. Wang, S. Yang, *et al.*, Preparation of Hollow Porous Carbon Nanofibers and Their Performance and Mechanism of Broadband Microwave Absorption, *Materials*, 2022, **15**(20), 7273.
52 I. Kiminaite, S. Wilhelm, L. Martetschlaeger, *et al.*, Plastic Devolatilisation Kinetics During Isothermal High-

Temperature Pyrolysis: Focus on Solid Products (Part I), *Polymers*, 2025, **17**(4), 525.

53 J. Lee and H. Lee, Valence State and Catalytic Activity of Ni-Fe Oxide Embedded in Carbon Nanotube Catalysts, *Nanomaterials*, 2024, **14**(24), 2004.

54 L. J. Tong, X. Lin, J. W. Cai, *et al.*, Effect of calcium ion concentration on the ORR performance of Pd/C catalysts, *RSC Adv.*, 2023, **13**(51), 36373–36381.

55 H. Begum, M. S. Ahmed and Y.-B. Kim, Nitrogen-rich graphitic-carbon®graphene as a metal-free electrocatalyst for oxygen reduction reaction, *Sci. Rep.*, 2020, **10**(1), 12431.

56 L. Rademacher, T. H. Y. Beglau, T. Heinen, *et al.*, Microwave-assisted synthesis of iridium oxide and palladium nanoparticles supported on a nitrogen-rich covalent triazine framework as superior electrocatalysts for the hydrogen evolution and oxygen reduction reaction, *Front. Chem.*, 2022, **10**, 945261.

57 I. Karajagi, K. Ramya, P. C. Ghosh, *et al.*, Co-doped carbon materials synthesized with polymeric precursors as bifunctional electrocatalysts, *RSC Adv.*, 2020, **10**(59), 35966–35978.

58 Y. Xi, Z. Lu, T. Bao, *et al.*, Photocatalytic H_2O_2 Production over Ultrathin Layered Double Hydroxide with 3.92% Solar-to-H_2O_2 Efficiency, *Nano-Micro Lett.*, 2026, **18**(1), 192.

59 Y. Zhao, Y. Lu, L. Chen, *et al.*, Redox Dual-Cocatalyst-Modified CdS Double-Heterojunction Photocatalysts for Efficient Hydrogen Production, *ACS Appl. Mater. Interfaces*, 2020, **12**(41), 46073–46083.

60 L. Xia, Y. Li, H. Song, *et al.*, MoO_2 nanosheets anchored with Co nanoparticles as a bifunctional electrocatalytic platform for overall water splitting, *RSC Adv.*, 2022, **12**(53), 34760–34765.